

# Potential window alignment regulating ion transfer in faradaic junctions for efficient photoelectrocatalysis

Received: 7 June 2023

Accepted: 24 November 2023

Published online: 02 December 2023

Check for updates

Hongzheng Dong<sup>1,5</sup>, Xiangyu Pan<sup>2,5</sup>, Yuancai Gong<sup>2</sup>, Mengfan Xue<sup>3</sup>, Pin Wang<sup>3</sup>, SocMan Ho-Kimura<sup>4</sup>, Yingfang Yao<sup>1</sup>, Hao Xin<sup>2</sup>✉, Wenjun Luo<sup>1</sup>✉ & Zhigang Zou<sup>1,3</sup>

In the past decades, a band alignment theory has become a basis for designing different high-performance semiconductor devices, such as photocatalysis, photoelectrocatalysis, photoelectrostorage and third-generation photovoltaics. Recently, a faradaic junction model (coupled electron and ion transfer) has been proposed to explain charge transfer phenomena in these semiconductor heterojunctions. However, the classic band alignment theory cannot explain coupled electron and ion transfer processes because it only regulates electron transfer. Therefore, it is very significant to explore a suitable design concept for regulating coupled electron and ion transfer in order to improve the performance of semiconductor heterojunctions. Herein, we propose a potential window alignment theory for regulating ion transfer and remarkably improving the photoelectrocatalytic performance of a MoS<sub>2</sub>/Cd-Cu<sub>2</sub>ZnSnS<sub>4</sub> heterojunction photocathode. Moreover, we find that a faradaic potential window, rather than the band position of the intermediate layer, is a criterion for identifying interface charge transfer direction. This finding can offer different perspectives for designing high-performance semiconductor heterojunctions with suitable potential windows for solar energy conversion and storage.

In the past several decades, photocatalysis, photoelectrocatalysis, photoelectrostorage, third-generation photovoltaics (such as quantum-dot or dye-sensitized, organic and perovskite solar cells) have attracted wide interest due to their low cost and high efficiency for converting solar energy into chemical or electric energy<sup>1–5</sup>. Among them, different kinds of heterojunctions, such as type-II heterojunction<sup>6</sup> and Z-scheme junction<sup>7</sup>, have been widely used to separate photo-excited carriers in light absorbers (Supplementary

Fig. 1). In all of these previous studies<sup>6–8</sup>, a band alignment theory is a basis for manipulating interface electron transfer in high-performance devices. However, Luo et al. have found that faradaic junction interface charge transfer process (coupled electron and ion transfer) widely exists in these solar energy conversion and storage devices<sup>9–17</sup>. Since the classic band alignment theory only regulates electron transfer, it is not suitable for explaining coupled electron and ion transfer in faradaic junctions. Therefore, it is very significant to explore a suitable

<sup>1</sup>Eco-materials and Renewable Energy Research Center (ERERC), National Laboratory of Solid State Microstructures, College of Engineering and Applied Sciences, Nanjing University, Nanjing 210093, China. <sup>2</sup>State Key Laboratory for Organic Electronics and Information Displays, College of Chemistry and Life Sciences, Nanjing University of Posts & Telecommunications, Nanjing 210023, China. <sup>3</sup>Eco-materials and Renewable Energy Research Center (ERERC), Jiangsu Key Laboratory for Nano Technology, National Laboratory of Solid State Microstructures and Department of Physics, Nanjing University, Nanjing 210093, China. <sup>4</sup>Institute of Applied Physics and Materials Engineering, University of Macau, Macau SAR, China. <sup>5</sup>These authors contributed equally: Hongzheng Dong, Xiangyu Pan. ✉e-mail: [iamhxin@njupt.edu.cn](mailto:iamhxin@njupt.edu.cn); [wjluo@nju.edu.cn](mailto:wjluo@nju.edu.cn)

design concept for regulating coupled electron and ion transfer in order to improve the performance of the semiconductor heterojunctions.

In this work, we have improved the photoelectrochemical hydrogen production performance of a  $\text{MoS}_2/\text{Cd-Cu}_2\text{ZnSnS}_4$  (CCZTS) heterojunction photocathode significantly by introducing an Au intermediate layer. However, a Pd intermediate layer with a similar Fermi level does not improve the performance of the same  $\text{MoS}_2/\text{CCZTS}$  heterojunction photocathode. The results suggest that the classic band alignment theory is not suitable for explaining the different effects of the Pd and Au layers on the photoelectrochemical properties of CCZTS. In order to investigate the reasons for the improved performance of  $\text{MoS}_2/\text{Au}/\text{CCZTS}$  heterojunction photocathode, some characterization methods, including in situ irradiated X-ray photoelectron spectra (XPS), quasi in situ irradiated Raman, in situ electrochemical Raman and time-of-flight secondary-ion mass spectrometry (TOF-SIMS), were carried out. We find that the  $\text{MoS}_2$  plays the role of recombination centers by a reversible faradaic reaction and decreases the performance of a  $\text{MoS}_2/\text{CCZTS}$  heterojunction photocathode. The introduction of the Au intermediate layer inhibits alkali metal ion intercalation reaction of  $\text{MoS}_2$  and decreases the recombination in the  $\text{MoS}_2/\text{CCZTS}$  heterojunction, but the Pd intermediate layer does not. Further studies suggest the Au layer indicates negligible reduction faradaic potential window, compared to the Pd layer, which suppresses alkali metal ion intercalation into  $\text{MoS}_2$ . Therefore, the theory of the potential window alignment can be used to explain the interface charge transfer in photoelectrocatalysis and can also provide guidance to improve the performance of photocatalysis, photoelectrostorage, third-generation photovoltaics and so on.

## Results

### The Au intermediate layer to improve photoelectrocatalytic performance of a $\text{MoS}_2/\text{CCZTS}$ heterojunction photocathode remarkably

In previous studies, Mo glass was widely used as a substrate for the preparation of a CCZTS thin film due to its good mechanical strength at high temperature<sup>18,19</sup>. Here, CCZTS films were deposited on Mo glass substrates by spin-coating and post-sulfurization method. After the sulfurization at high temperature,  $\text{MoS}_2$  was inevitably in situ produced on the surface of Mo glass substrates, which contacts with CCZTS to form  $\text{MoS}_2/\text{CCZTS}$  heterojunction<sup>20,21</sup>. For  $\text{MoS}_2/\text{Pd}/\text{CCZTS}$  and  $\text{MoS}_2/\text{Au}/\text{CCZTS}$  samples, Pd and Au intermediate layers were deposited firstly on Mo glass substrates with an ion beam sputtering method and then CCZTS layers were prepared. The preparation details of the three samples can be found in the Methods section. The three samples were characterized by XRD (Supplementary Fig. 2a). The diffraction peaks at  $28.4^\circ$ ,  $47.3^\circ$  and  $56.2^\circ$  correspond to the (112), (220) and (312) planes of kesterite CCZTS<sup>22,23</sup>, and the peaks of Au can also be observed in  $\text{MoS}_2/\text{Au}/\text{CCZTS}$  sample. However, no diffraction peaks of Pd and  $\text{MoS}_2$  are observed in the three samples by the conventional XRD method due to their poor crystallinity. In order to further identify the Pd and  $\text{MoS}_2$ , the CCZTS layers were removed by a tweezer and Grazing Incidence X-Ray Diffraction (GIXRD) was used to characterize the exposed  $\text{MoS}_2$  and  $\text{MoS}_2/\text{Pd}$  substrates (Supplementary Fig. 2b). By this method, the diffraction peaks of Pd and 2H- $\text{MoS}_2$  are observed. Figure 1a–c show the cross-sectional SEM images of  $\text{MoS}_2/\text{CCZTS}$ ,  $\text{MoS}_2/\text{Pd}/\text{CCZTS}$  and  $\text{MoS}_2/\text{Au}/\text{CCZTS}$ , respectively. In the three samples, well-grown CCZTS grains with different sizes are packed on the substrates. Therefore, the Pd and Au intermediate layers do not change the morphologies of CCZTS obviously. Moreover, both Pd and

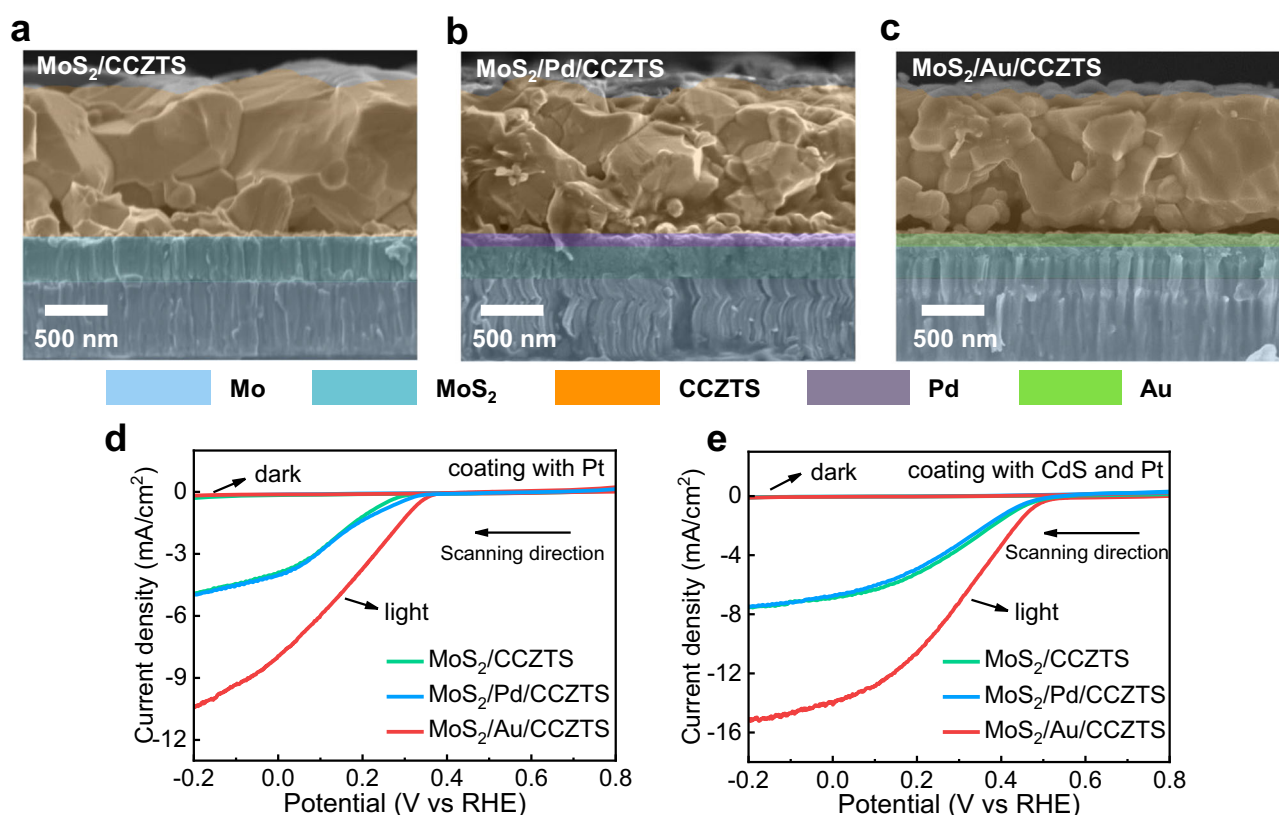


**Fig. 1 | Characterization and photocurrent of  $\text{MoS}_2/\text{CCZTS}$ ,  $\text{MoS}_2/\text{Pd}/\text{CCZTS}$  and  $\text{MoS}_2/\text{Au}/\text{CCZTS}$  samples. a–c** The cross-sectional SEM images of  $\text{MoS}_2/\text{CCZTS}$  (a),  $\text{MoS}_2/\text{Pd}/\text{CCZTS}$  (b) and  $\text{MoS}_2/\text{Au}/\text{CCZTS}$  (c). **d, e** Linear sweep voltammetry curves of  $\text{MoS}_2/\text{CCZTS}$ ,  $\text{MoS}_2/\text{Pd}/\text{CCZTS}$  and  $\text{MoS}_2/\text{Au}/\text{CCZTS}$  after

coating a Pt co-catalyst (d) or coating a CdS buffer layer and a Pt co-catalyst (e); Scan rate of 10 mV/s; Electrolyte: 0.2 M  $\text{Na}_2\text{HPO}_4/\text{NaH}_2\text{PO}_4$  aqueous solution (pH = 6.5). Light source: an AM 1.5 G sunlight simulator, light intensity: 100 mW/cm<sup>2</sup>.

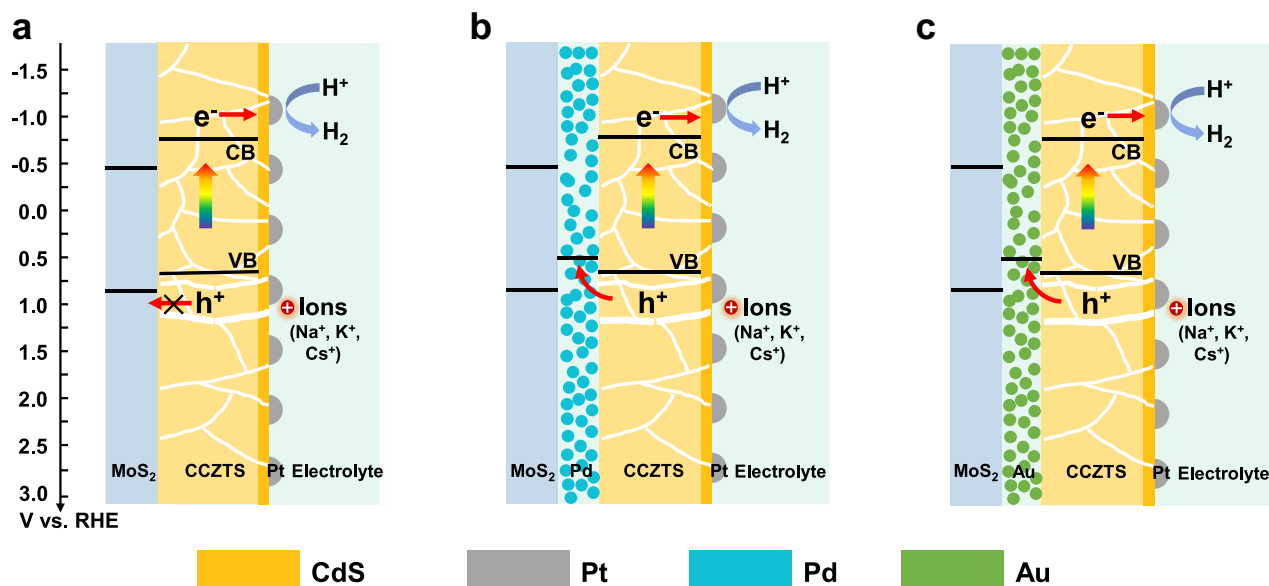


**Fig. 2 | Conventional band alignment theory for interface charge transfer.** a–c The diagram of interface charge transfer in MoS<sub>2</sub>/CCZTS (a), MoS<sub>2</sub>/Pd/CCZTS (b) and MoS<sub>2</sub>/Au/CCZTS (c) heterojunction photocathodes.

Au intermediate layers between MoS<sub>2</sub> and CCZTS indicate small particle aggregates, which are about 80 nm in thickness (Supplementary Figs. 3, 4) and cover the MoS<sub>2</sub> underlayers incompletely in the heterojunctions from the top-view SEM images by removing the upper layers of CCZTS (Supplementary Fig. 5).

In order to investigate the effects of Pd and Au intermediate layers on the photoelectrochemical performance of CCZTS-based photocathodes, the photocurrent density of MoS<sub>2</sub>/CCZTS, MoS<sub>2</sub>/Pd/CCZTS and MoS<sub>2</sub>/Au/CCZTS samples were measured in 0.2 M Na<sub>2</sub>HPO<sub>4</sub>/NaH<sub>2</sub>PO<sub>4</sub> aqueous solution. From previous studies<sup>24</sup>, the photocurrent of the bare CCZTS sample is negligible due to its low electrocatalytic activity for hydrogen production. Therefore, Pt co-catalysts were loaded on the surfaces of the three samples by an ion beam sputtering method for photoelectrocatalytic measurement. Figure 1d indicates Linear sweep voltammetry (LSV) curves of the three samples with Pt cocatalysts. Usually, a more negative potential has a larger driving force for electron-hole separation in a photocathode, which will lead to a higher photocurrent at a more negative potential. Therefore, the photocurrent of all of the three samples increases with shifting the potential negatively. It is worth noting that the photocurrent of CCZTS increases significantly after introducing the Au layer. In contrast, the MoS<sub>2</sub>/Pd/CCZTS exhibits a similar photocurrent to that of the MoS<sub>2</sub>/CCZTS photocathode. Moreover, n-CdS was also introduced as a buffer layer between CCZTS and Pt co-catalysts to further improve the photoelectrocatalytic performance<sup>22,23</sup>. The photocurrent density of MoS<sub>2</sub>/CCZTS increases from 7.2 mA/cm<sup>2</sup> to 14.9 mA/cm<sup>2</sup> @ 0 V<sub>RHE</sub> after introducing the Au intermediate layer, but slightly decreases after introducing the Pd layer (Fig. 1e), which is further confirmed by the statistical results in the Supplementary Fig. 6. Moreover, the three samples also indicate good stability under illumination and the photocurrents only decay by about 5–11% after 3600 s of illumination (Supplementary Fig. 7). Therefore, the Au intermediate layer can improve the photoelectrocatalytic performance of the MoS<sub>2</sub>/CCZTS heterojunction photocathode remarkably.

In order to investigate the reason that enhanced photocurrent is only observed in MoS<sub>2</sub>/Au/CCZTS heterojunction photocathode, but not in MoS<sub>2</sub>/Pd/CCZTS, we measured the substrate resistance and light absorption of the samples and the results are shown in Supplementary Table 1 and Supplementary Fig. 8, respectively. The MoS<sub>2</sub>/Au substrate exhibits similar resistance as the MoS<sub>2</sub>/Pd substrate and the light

absorption of CCZTS does not change obviously on different substrates, suggesting that the difference in performance of these samples does not come from the change of the substrate resistance and light absorption. Since a band alignment theory is usually used to understand the improved performance in the heterojunction, the band gaps and band positions of four CCZTS and MoS<sub>2</sub> samples were measured by UV-vis spectra and Mott-Schottky methods, respectively (Supplementary Figs. 9, 10). The average values and errors of the band gaps and band positions of the four samples are calculated and shown in Supplementary Table 2, which are in good agreement with some previous reports<sup>23,25</sup>. Moreover, the Fermi levels ( $E_F$ ) of Pd and Au particulate films in this study were obtained by ultraviolet photoelectron spectroscopy (Supplementary Fig. 11) and the values are summarized in Supplementary Table 3, which are similar to the reference values in previous studies<sup>26,27</sup>. According to the above values, the band positions of MoS<sub>2</sub>/CCZTS, MoS<sub>2</sub>/Pd/CCZTS and MoS<sub>2</sub>/Au/CCZTS heterojunction photocathodes are plotted in Fig. 2. Based on the band alignment theory, the valence band of CCZTS is higher than that of MoS<sub>2</sub>, unfavorable for photo-generated hole transferring from the CCZTS photocathode to MoS<sub>2</sub>. Therefore, the Pd or Au intermediate layers with the higher Fermi level will be helpful for hole transfer from CCZTS to the metal layers, which can improve the performance of a CCZTS photocathode<sup>28</sup>. However, in experiments, not the Pd but the Au intermediate layer improves the photocurrent for solar hydrogen production. Therefore, the classic band alignment theory is not suitable for explaining the converse effects of the Pd and Au layers on the photoelectrochemical properties of CCZTS.

### The Au intermediate layer to regulate ion transfer in the MoS<sub>2</sub>/CCZTS heterojunction photocathode under illumination

According to previous studies<sup>9–16</sup>, a faradaic junction charge transfer widely exists in different heterojunctions. Herein, we investigated the effects of Pd and Au on interface charge transfer in MoS<sub>2</sub>/CCZTS by in situ irradiated XPS and the experimental details are shown in Supplementary Fig. 12. Since XPS is a surface characterization technique, it is difficult to obtain the Mo signal in the substrate if the CCZTS upper layer is too thick and compact. A thinner and porous CCZTS upper layer was prepared by only reducing the number of coating layers from seven to two with the same method, and the XPS peak of Mo 3d becomes more intensive in the MoS<sub>2</sub>/CCZTS sample (Supplementary

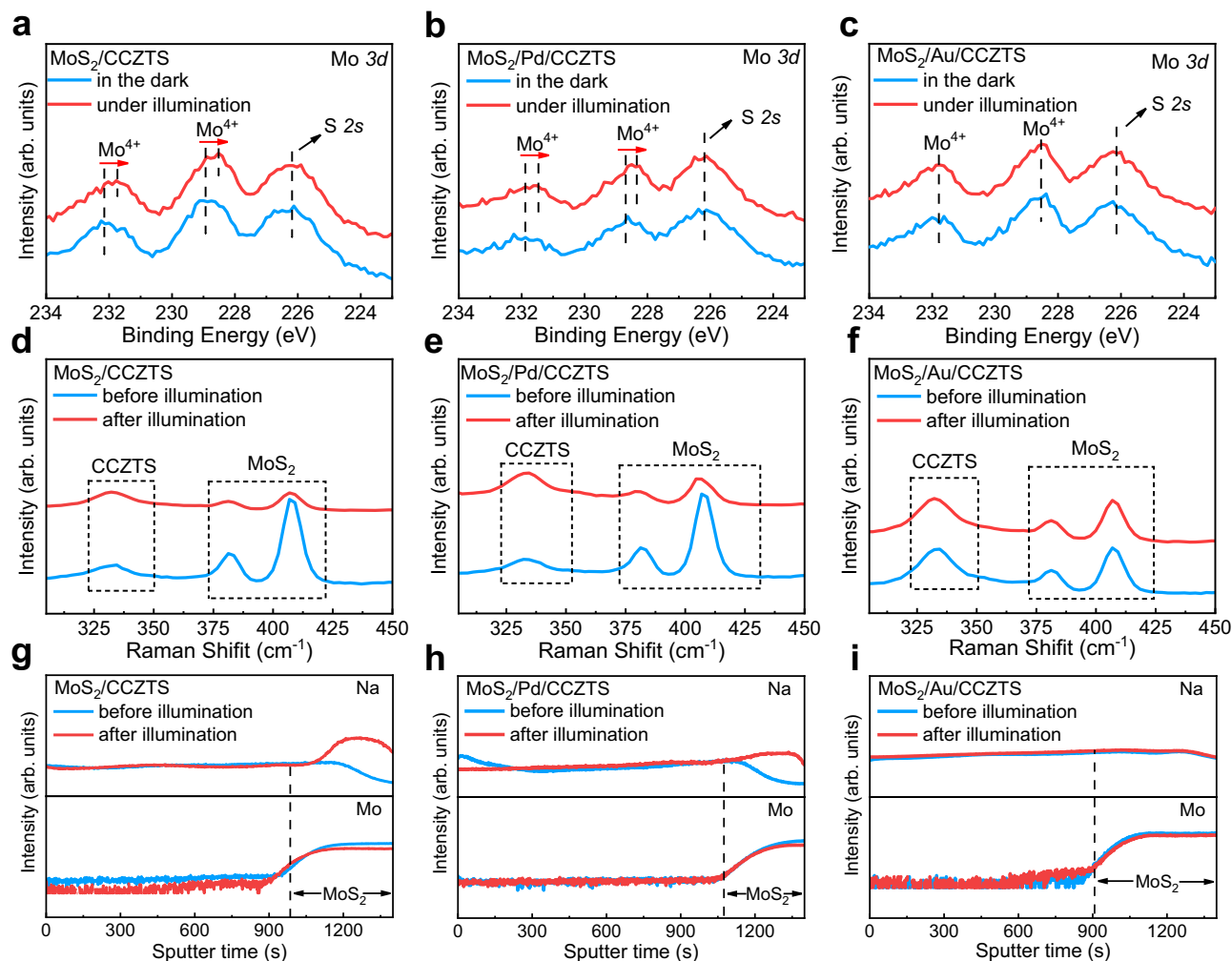


**Fig. 3 | Interface charge transfer process in MoS<sub>2</sub>/CCZTS, MoS<sub>2</sub>/Pd/CCZTS and MoS<sub>2</sub>/Au/CCZTS samples.** **a–c** In situ irradiated XPS spectra of Mo 3d in MoS<sub>2</sub>/CCZTS (**a**), MoS<sub>2</sub>/Pd/CCZTS (**b**) and MoS<sub>2</sub>/Au/CCZTS (**c**) in the dark and under full arc Xe lamp illumination. The coating and annealing were repeated two times to obtain a detectable XPS signal of Mo. **d–f** Quasi in situ irradiated Raman spectra of

MoS<sub>2</sub>/CCZTS (**d**), MoS<sub>2</sub>/Pd/CCZTS (**e**) and MoS<sub>2</sub>/Au/CCZTS (**f**) in the electrolyte before and after full arc Xe lamp illumination. **g–i** Secondary ion intensities of Na and Mo ions in MoS<sub>2</sub>/CCZTS (**g**), MoS<sub>2</sub>/Pd/CCZTS (**h**) and MoS<sub>2</sub>/Au/CCZTS (**i**) junctions in the electrolyte before and after full arc Xe lamp illumination. Electrolyte: 0.2 M Na<sub>2</sub>HPO<sub>4</sub>/NaH<sub>2</sub>PO<sub>4</sub> aqueous solution; Light source: a full arc Xe lamp.

Fig. 13). Therefore, the MoS<sub>2</sub>/CCZTS sample with two coating layers was investigated by in situ irradiated XPS and the results are shown in Fig. 3a–c. Two binding energies at 231.9 eV and 228.8 eV are assigned as Mo<sup>4+</sup> in the MoS<sub>2</sub>/CCZTS sample in the dark (Fig. 3a), which shift to lower values under illumination<sup>29</sup>. The results suggest that Mo<sup>4+</sup> ions are photo-reduced into lower valence states<sup>30</sup>. After introducing Pd and Au intermediate layers, lower binding energies of Mo are only observed in MoS<sub>2</sub>/Pd/CCZTS, but not in MoS<sub>2</sub>/Au/CCZTS under illumination (Fig. 3b, c). The results suggest that the Au rather than Pd intermediate layer can prevent the reduction of Mo<sup>4+</sup> in the MoS<sub>2</sub>/CCZTS junction. On the other hand, the binding energies of Cu 2p, Zn 2p, Sn 3d and S 2p in the three samples do not shift under illumination, suggesting that the CCZTS does not change (Supplementary Figs. 14–16). Quasi in situ irradiated Raman spectra were also used to investigate the effects of Au and Pd on the reduction process of MoS<sub>2</sub> in MoS<sub>2</sub>/CCZTS before and after illumination<sup>31</sup> and the experimental details are shown in Supplementary Fig. 17. The Raman peaks at 382 cm<sup>-1</sup> and 408 cm<sup>-1</sup> are assigned as E<sub>2g</sub> and A<sub>1g</sub> vibrational modes of MoS<sub>2</sub>, and the peak at 332 cm<sup>-1</sup> corresponds to CCZTS<sup>22,29</sup>. After MoS<sub>2</sub>/CCZTS is illuminated, the Raman peak intensity of CCZTS does not change, while the Raman peak intensity of MoS<sub>2</sub> decreases (Fig. 3d). In contrast, the Raman peak intensity of MoS<sub>2</sub> film alone does not

decrease after the same illumination (Supplementary Fig. 18). Therefore, interface charge transfer in the MoS<sub>2</sub>/CCZTS heterojunction under illumination leads to the change of the Raman peak intensity of MoS<sub>2</sub>. According to previous studies<sup>32,33</sup>, the decrease of Raman peak intensity of MoS<sub>2</sub> can be attributed to the Na<sup>+</sup> intercalation into MoS<sub>2</sub>. The Raman peak intensity of MoS<sub>2</sub> decreases in MoS<sub>2</sub>/Pd/CCZTS but not in MoS<sub>2</sub>/Au/CCZTS after illumination (Fig. 3e, f). The results further suggest that the Au rather than Pd intermediate layer can inhibit the reduction intercalation reaction of MoS<sub>2</sub> in the MoS<sub>2</sub>/CCZTS junction, which are in good agreement with in situ irradiated XPS results mentioned above.

In order to further investigate the effects of Au and Pd on interface ion transfer in MoS<sub>2</sub>/CCZTS under illumination, time-of-flight secondary ion mass spectrometry (TOF-SIMS) depth profiles were used to identify the element distribution in the three samples in 0.2 M Na<sub>2</sub>HPO<sub>4</sub>/NaH<sub>2</sub>PO<sub>4</sub> aqueous solution before and after illumination. Before illumination, Na<sup>+</sup> ions uniformly distribute in the bulk of the CCZTS film and decrease at the MoS<sub>2</sub>/CCZTS interface. After illumination, the distribution of Cu, Zn, Sn and S in CCZTS does not change obviously (Supplementary Fig. 19), while the intensity of Na<sup>+</sup> ions enhances remarkably at the depth of sputtering time >980 s in the sample (Fig. 3g), where the MoS<sub>2</sub> is located. Since some pin holes

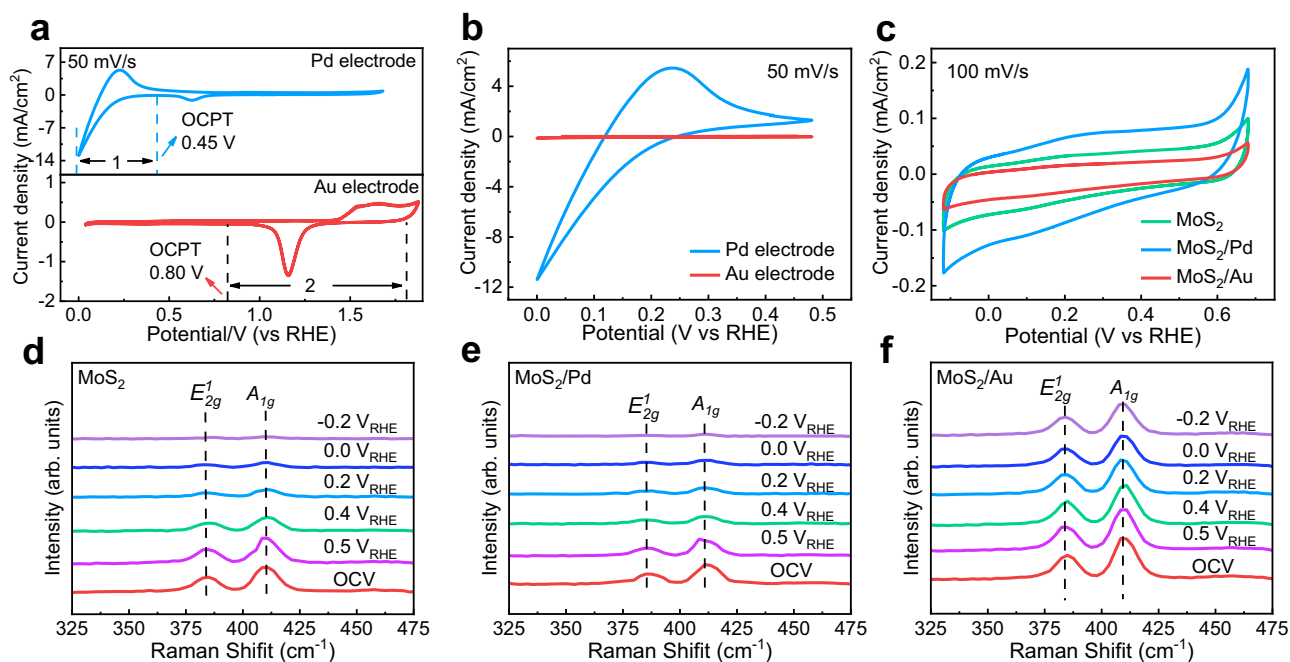


**Fig. 4** | The reasons of Au rather than Pd to inhibit Na<sup>+</sup> intercalation into MoS<sub>2</sub>. **a–c** Cyclic voltammetry curves of Pd and Au electrodes (**a**, **b**), MoS<sub>2</sub>, MoS<sub>2</sub>/Pd and MoS<sub>2</sub>/Au (**c**) in the electrolyte in the dark. **d–f** In situ electrochemical Raman

spectra of MoS<sub>2</sub> (**d**), MoS<sub>2</sub>/Pd (**e**) and MoS<sub>2</sub>/Au (**f**) in the electrolyte at different potentials in the dark. Electrolyte: 0.2 M Na<sub>2</sub>HPO<sub>4</sub>/NaH<sub>2</sub>PO<sub>4</sub> aqueous solution.

inevitably exist even in the dense and thick CCZTS films prepared by the spin-coating method, electrolyte can penetrate into the MoS<sub>2</sub> layer through the pin holes (Supplementary Fig. 20). Therefore, the Na<sup>+</sup> intercalation into MoS<sub>2</sub> happens in the MoS<sub>2</sub>/CCZTS sample in the electrolyte under illumination. According to in situ irradiated XPS and TOF-SIMS, the MoS<sub>2</sub>/CCZTS is a faradaic junction with the interface reaction of MoS<sub>2</sub> + x Na<sup>+</sup> + x e<sup>-</sup> ↔ Na<sub>x</sub>MoS<sub>2</sub>. In the MoS<sub>2</sub>/Pd/CCZTS junction, similar Na<sup>+</sup> intercalation into MoS<sub>2</sub> was observed after illumination (Fig. 3h and Supplementary Fig. 21). In contrast, the distribution of Na<sup>+</sup> in the MoS<sub>2</sub>/Au/CCZTS junction does not change after illumination (Fig. 3i and Supplementary Fig. 22). Therefore, the Na<sup>+</sup> intercalation into MoS<sub>2</sub> is suppressed only by the Au rather than Pd intermediate layer in MoS<sub>2</sub>/CCZTS.

In order to further understand why the Au layer, not the Pd layer, can inhibit the faradaic reaction of MoS<sub>2</sub>, the electrochemical behavior of Pd and Au were measured and the results are shown in Fig. 4a. According to previous studies<sup>34,35</sup>, the faradaic potential window is defined as a potential range in which a material exhibits stable and reversible electrochemical faradaic redox reactions in the electrolyte. Therefore, a Pd electrode indicates a reduction faradaic potential window<sup>16,36,37</sup>, which is assigned as Pd + x H<sup>+</sup> + x e<sup>-</sup> ↔ β-PdH<sub>x</sub> (1). Different from a Pd electrode, an Au electrode only exhibits an oxidation faradaic potential window, Au + H<sub>2</sub>O ↔ Au-O + 2 H<sup>+</sup> + 2 e<sup>-</sup> (2). Since MoS<sub>2</sub> is reduced by photo-generated electrons in CCZTS, enlarged reduction faradaic potential windows of Pd and Au are shown in Fig. 4b. A Pd electrode indicates a reduction faradaic potential window of 0 V<sub>RHE</sub> to 0.45 V<sub>RHE</sub>, while the Au electrode indicates a negligible reduction faradaic capacitance at the same potential window. It is because the lower adsorption energy of H<sup>+</sup> on the surface of Pd than on the Au layer, which leads to a much higher capacitance of Pd than Au<sup>38,39</sup>. In order to investigate the effects of the coating of Pd and Au on the faradaic capacitance of MoS<sub>2</sub> (Supplementary Fig. 24), the cyclic voltammetry curves of MoS<sub>2</sub>, MoS<sub>2</sub>/Pd and MoS<sub>2</sub>/Au were measured in the same electrolyte and the results are shown in Fig. 4c. The faradaic capacitance of MoS<sub>2</sub> increases after the coating of a Pd layer, but decreases obviously after coating the Au layer. In order to further elucidate the reasons of Au not Pd inhibiting

Na<sup>+</sup> intercalation, in situ electrochemical Raman spectroscopy was carried out to investigate the change of MoS<sub>2</sub>, MoS<sub>2</sub>/Pd and MoS<sub>2</sub>/Au samples during electrochemical measurement and the experimental details are shown in Supplementary Fig. 25. The Raman peak intensity of MoS<sub>2</sub> does not change obviously at the potential of 0.5 V<sub>RHE</sub>, and decreases from 0.4 V<sub>RHE</sub> to negligible at -0.2 V<sub>RHE</sub> (Fig. 4d). Therefore, Na<sup>+</sup> intercalation in MoS<sub>2</sub> becomes more intense with the potential shifting negatively, consistent with the previous study<sup>33</sup>. The Raman peak intensity of MoS<sub>2</sub> in a MoS<sub>2</sub>/Pd sample also decreases with the potential shifting negatively, but changes only slightly in MoS<sub>2</sub>/Au (Fig. 4e, f). In a MoS<sub>2</sub>/Pd sample, after the reduction adsorption of H<sup>+</sup> on Pd (Pd + x H<sup>+</sup> + x e<sup>-</sup> ↔ β-PdH<sub>x</sub>), interface charges can transfer from Pd to MoS<sub>2</sub> following the reaction of MoS<sub>2</sub> + x Na<sup>+</sup> + β-PdH<sub>x</sub> ↔ Na<sub>x</sub>MoS<sub>2</sub> + Pd + x H<sup>+</sup>. In contrast, there is negligible reduction adsorption of H<sup>+</sup> on an Au layer, which leads to Na<sup>+</sup> intercalation being suppressed into MoS<sub>2</sub>. Therefore, the Au layer plays the role of an ion blocking layer in the heterojunction photocathode. In order to further confirm the effects of an ion blocking layer, the photoelectrocatalytic performances of the MoS<sub>2</sub>/CCZTS, MoS<sub>2</sub>/Pd/CCZTS and MoS<sub>2</sub>/Au/CCZTS photocathodes were also measured in the electrolytes with different alkali metal ions (Na<sup>+</sup>/K<sup>+</sup>/Cs<sup>+</sup>) (Supplementary Figs. 26–29). The results suggest that the intercalation reaction of MoS<sub>2</sub> can also be suppressed with increasing alkali metal ion radii in the electrolytes and improve the photoelectrocatalytic performance of the three heterojunction photocathodes. Especially, the MoS<sub>2</sub>/Au/CCZTS photocathode indicates a high photocurrent of 16.3 mA/cm<sup>2</sup> at 0 V<sub>RHE</sub> in the electrolyte with Cs<sup>+</sup>, which is close to the highest value in the neutral aqueous solution (Supplementary Table 4). Therefore, the photoelectrocatalytic performance of the heterojunction photocathodes can be improved remarkably by regulating ion transfer. So far, there are some reports on improving the performance of photoelectrocatalytic cells and dye-sensitized solar cells by adjusting the concentrations and species of ions in the electrolytes<sup>40,41</sup>. However, most of these previous studies only focus on the effects of various electrolytes on the properties of an individual catalyst or semiconductor, but not interface charge transfer in the heterojunctions. This work provides a different paradigm of

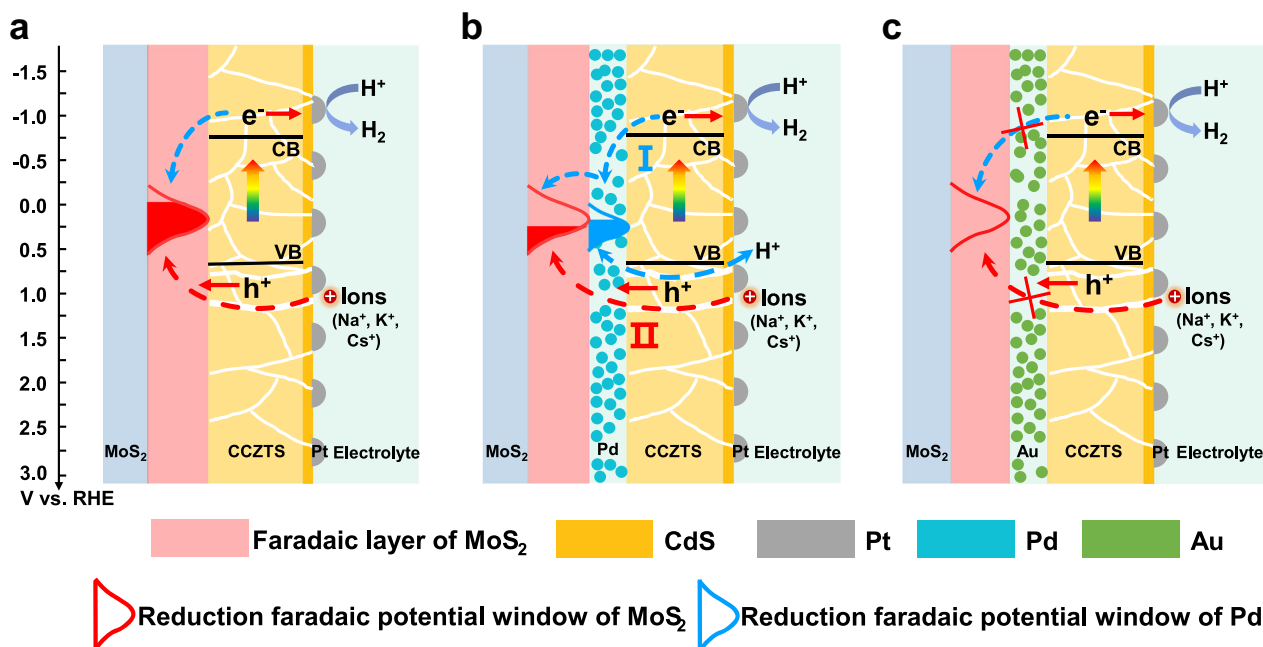


**Fig. 5 | The mechanism of Au to improve the photoelectrocatalytic performance of a MoS<sub>2</sub>/CCZTS heterojunction photocathode. a–c** Interface charge transfer in MoS<sub>2</sub>/CCZTS (a), MoS<sub>2</sub>/Pd/CCZTS (b) and MoS<sub>2</sub>/Au/CCZTS (c) heterojunction photocathodes after coating a CdS buffer layer and a Pt co-catalyst.

regulating ion transfer to design high-performance semiconductor heterojunctions.

#### Potential window alignment to improve photoelectrocatalytic performance in a MoS<sub>2</sub>/Au/CCZTS heterojunction photocathode

According to the above results and analysis, we propose a mechanism for the improved performance of MoS<sub>2</sub>/CCZTS after introducing the Au intermediate layer. According to the above results (Supplementary Figs. 9, 10, 24), the band positions of semiconductors and the faradaic potential windows of MoS<sub>2</sub>, Pd and Au are plotted in Fig. 5. When the conduction band of CCZTS is higher than the faradaic potential window of MoS<sub>2</sub>, part of the photo-generated electrons in CCZTS can reduce H<sup>+</sup> into hydrogen, and the other electrons reduce the MoS<sub>2</sub> with the intercalation of Na<sup>+</sup> (K<sup>+</sup>/Cs<sup>+</sup>) from the electrolyte. Moreover, part of photo-excited holes can re-oxidize the Na<sub>x</sub>MoS<sub>2</sub> (K<sub>x</sub>MoS<sub>2</sub> or Cs<sub>x</sub>MoS<sub>2</sub>) during the transfer process. Therefore, the MoS<sub>2</sub> plays the role of recombination centers, which decreases the photocurrent of the MoS<sub>2</sub>/CCZTS sample (Fig. 5a). Since a Pd intermediate layer indicates a similar reduction faradaic window position with MoS<sub>2</sub>, the photo-generated electrons in CCZTS can transfer to Pd and induce the H<sup>+</sup> adsorption reaction to form β-PdH<sub>x</sub>, which can further reduce MoS<sub>2</sub> and is recovered into Pd. The charge transfer at MoS<sub>2</sub>/Pd interface follows the reaction of MoS<sub>2</sub> + x Na<sup>+</sup> (K<sup>+</sup>/Cs<sup>+</sup>) + β-PdH<sub>x</sub> ↔ Na<sub>x</sub>MoS<sub>2</sub> (K<sub>x</sub>MoS<sub>2</sub>/Cs<sub>x</sub>MoS<sub>2</sub>) + Pd + x H<sup>+</sup>, which leads to a higher capacitance and a lower photocurrent in MoS<sub>2</sub>/Pd/CCZTS. However, the Au intermediate layer can inhibit the Na<sup>+</sup> intercalation into MoS<sub>2</sub> and improve the performance of the MoS<sub>2</sub>/CCZTS sample. These results suggest that a faradaic potential window, not a Fermi level, is a criterion for interface charge transfer direction in a faradaic junction. The driving force for charge separation in a faradaic junction is the difference of electrochemical potential at the interface, which is intrinsically different from the built-in electric field in a physical heterojunction based on classic band theory<sup>9–16</sup>.

#### Discussion

In summary, by introducing the Pd and Au intermediate layers in MoS<sub>2</sub>/CCZTS, the photocurrent increases obviously in MoS<sub>2</sub>/Au/CCZTS, but

decreases slightly in MoS<sub>2</sub>/Pd/CCZTS. It is because the Au layer acts as an ion blocking layer to inhibit the recombination of photo-generated carriers and improve the photocurrent. Moreover, we find that it is the potential windows not the band positions of the intermediate layer that is the criterion for controlling interface charge transfer direction in a faradaic junction. The potential window alignment theory cannot only deepen the understanding of interface charge transfer in the heterojunction but also offer a suitable design concept for improving the performance of other solar energy conversion and storage devices, such as photocatalysis, photoelectrocatalysis, photoelectrostorage and third-generation photovoltaics.

#### Methods

##### Preparation of the precursor solution

The precursor solution was prepared in a glovebox with O<sub>2</sub> and H<sub>2</sub>O level below 5 ppm at room temperature similar to previous reports<sup>19,42</sup>. First, 4 mL of DMSO (99.8%, J&K) was added to a glass vial by a syringe followed by adding 2.4785 g of thiourea (Tu, 99%, Aladdin, recrystallized twice) and 0.7405 g of CuCl (99.999%, Alfa); Second, 1.0420 g of SnCl<sub>4</sub> (99.99%, Alfa) was added to a second vial followed by adding 4 mL of DMSO, 0.6165 g of Zn(OAc)<sub>2</sub> (99.99%, Aladdin), and 0.2638 g of CdCl<sub>2</sub> (99.99%, Aladdin). The two vials were mixed and stirred until clear. The mole ratios of the elements in the solution are Cu/(Zn + Cd + Sn) = 0.85, (Zn + Cd)/Sn = 1.20, Cd/(Zn + Cd) = 0.30.

##### Fabrication of the CCZTS absorber film

The glass/Mo/Pd and glass/Mo/Au substrates were prepared by depositing Pd films or Au films on Mo glass substrates using an ion beam sputtering method at room temperature for 15 min. To obtain CCZTS precursor thin film, the precursor solution was spin coated on glass/Mo, glass/Mo/Pd, or glass/Mo/Au substrates at 2000 rpm for 60 s. After spin-coating, the films were immediately annealed at 370 °C for 90 s on a hot plate and then cooled down. The coating and annealing were repeated seven times in order to obtain a desired absorber layer thickness in the glovebox. The films were placed in a graphite box with 100 mg of sulfur powder and 100 mg of stannous sulfide and the graphite box was placed in a rapid thermal processing (RTP) tube furnace for sulfurization. The tube was pumped and refilled

with Argon three times before heated up. The furnace was heated to 620 °C from room temperature over a period of 20 min. The sulfuration was performed at this temperature for 15 minutes and cooled to room temperature naturally.

### Coating of a CdS buffer layer and a Pt co-catalyst on CCZTS films

A CdS buffer layer was deposited on the CCZTS surface by a chemical bath deposition method. Specifically, the CCZTS samples were immersed in aqueous solution containing 1.5 mM CdSO<sub>4</sub>, 75 mM SC(NH<sub>2</sub>)<sub>2</sub> and 2.3 M NH<sub>3</sub>·H<sub>2</sub>O. The deposition temperature was 60 °C and the deposition time was 5 min. Then, a Pt co-catalyst was deposited on the surface of CdS/CCZTS using an ion beam sputtering method at room temperature for 25 s.

### Characterization of samples

The crystalline structures of the three samples were characterized by X-ray diffraction (XRD smartlab, 9 kW). After CCZTS were scraped off the substrate with a tweezer, the MoS<sub>2</sub>, MoS<sub>2</sub>/Pd and MoS<sub>2</sub>/Au substrates were characterized by Grazing Incidence X-Ray Diffraction (GIXRD) (Rigaku Smart lab X-ray diffractometer), four-point probe (Summit 11000 m) and scanning electron microscope (SEM, Gemini500). The cross-section and top-view morphologies of the MoS<sub>2</sub>/CCZTS, MoS<sub>2</sub>/Pd/CCZTS and MoS<sub>2</sub>/Au/CCZTS samples were observed by SEM. The element distribution of the thick and dense CCZTS samples before and after illumination in the electrolyte were identified by time-of-flight secondary ion mass spectrometry (TOF-SIMS 5 iontof, PHI NanoTOFII). The absorption spectra of the samples were recorded by a UV-visible-NIR spectrophotometer (PE lambda 950). The Mott-Schottky plots of CCZTS and MoS<sub>2</sub> samples were measured in a cell with a carbon rod and a saturated Ag/AgCl electrode as the counter and reference electrode, respectively. An electrochemical analyzer (CHI 760e, Shanghai Chenhua) was used to control the potentials of CCZTS and MoS<sub>2</sub> samples with an a.c. amplitude of 5 mV and a frequency of 1000 Hz. For ultraviolet photoelectron spectra (UPS) measurement, the Pd and Au films were deposited on glass substrates by an ion beam sputtering method for 15 min and the photoelectron spectra of the films were performed in a Kratos Ultra Spectrometer (K-ALPHA+, Thermo Fisher) by using a He I (21.22 eV) discharge lamp.

### In situ irradiated XPS, in situ electrochemical Raman and quasi in situ irradiated Raman characterization of samples

In situ irradiated X-ray photoelectron spectra were measured under a full arc Xe lamp with a XPS spectrometer (Thermofisher Escalab 250Xi). Since the CCZTS layer can attenuate XPS intensity of MoS<sub>2</sub>, a thin and porous CCZTS were prepared by coating and annealing for two times. For in situ irradiated XPS measurement, the MoS<sub>2</sub>/CCZTS, MoS<sub>2</sub>/Pd/CCZTS and MoS<sub>2</sub>/Au/CCZTS samples were pretreated by immersing them in 0.2 M Na<sub>2</sub>HPO<sub>4</sub>/NaH<sub>2</sub>PO<sub>4</sub> aqueous solution and exposing them to water vapor. In order to investigate the charge transfer in the three samples, in situ XPS was measured in the dark and after 10-mins' illumination. In situ electrochemical Raman spectra (Horiba T64000, excitation wavelength -488 nm) were measured in a cell with a saturated Ag/AgCl electrode and a Pt wire as a reference and a counter electrode, respectively. The potential of the MoS<sub>2</sub>, MoS<sub>2</sub>/Pd and MoS<sub>2</sub>/Au was applied by an electrochemical analyzer (CHI-760E, Shanghai Chenhua). Raman signals were detected simultaneously when the electrochemical curves of the samples were measured in the dark. An aqueous solution of 0.2 M Na<sub>2</sub>HPO<sub>4</sub>/NaH<sub>2</sub>PO<sub>4</sub> (K<sub>2</sub>HPO<sub>4</sub>/KH<sub>2</sub>PO<sub>4</sub> or Cs<sub>2</sub>HPO<sub>4</sub>/CsH<sub>2</sub>PO<sub>4</sub>) was used as electrolyte. Quasi in situ irradiated Raman spectra of thick and dense CCZTS samples on different substrates were measured before and after illumination by a Xe lamp in 0.2 M Na<sub>2</sub>HPO<sub>4</sub>/NaH<sub>2</sub>PO<sub>4</sub> aqueous solution.

### Photoelectrochemical measurement

The photoelectrochemical performance was measured in a conventional three-electrode cell using an electrochemical analyzer (CHI-760E, Shanghai Chenhua) with an AM 1.5 G sunlight simulator (CEL-AAAS50, 100 mW/cm<sup>2</sup>, China Education Au-light). A carbon rod and a saturated Ag/AgCl electrode were employed as the counter and the reference electrode, respectively. The electrolyte was the aqueous solution of 0.2 M Na<sub>2</sub>HPO<sub>4</sub>/NaH<sub>2</sub>PO<sub>4</sub> (K<sub>2</sub>HPO<sub>4</sub>/KH<sub>2</sub>PO<sub>4</sub> and Cs<sub>2</sub>HPO<sub>4</sub>/CsH<sub>2</sub>PO<sub>4</sub>). The potentials of working electrode were converted to reversible hydrogen electrode by the following formula:  $V_{RHE} = V_{Ag/AgCl} + 0.199 V + 0.059 * pH$ . The incident photon-to-current efficiency (IPCE) was obtained under irradiation of different wavelengths of light and was calculated by the following formula:

$$IPCE = \frac{1240 * I_{ph}}{P * \lambda}$$

Where the  $I_{ph}$  is the photocurrent density obtained at the potential of 0  $V_{RHE}$ ,  $P$  and  $\lambda$  are the power density ( $\mu W/cm^2$ ) and wavelength ( $\mu W/cm^2$ ) of the incident light, respectively.

### Data availability

All data are available in the main text or the Supplementary Information files. Additional data related to the findings of this study are available from the corresponding author upon reasonable request.

### References

- Kosco, J. et al. Enhanced photocatalytic hydrogen evolution from organic semiconductor heterojunction nanoparticles. *Nat. Mater.* **19**, 559–565 (2020).
- Pan, L. et al. Boosting the performance of Cu<sub>2</sub>O photocathodes for unassisted solar water splitting devices. *Nat. Catal.* **1**, 412–420 (2018).
- Li, W. et al. High-performance solar flow battery powered by a perovskite/silicon tandem solar cell. *Nat. Mater.* **19**, 1326–1331 (2020).
- Chuang, C.-H. M., Brown, P. R., Bulović, V. & Bawendi, M. G. Improved performance and stability in quantum dot solar cells through band alignment engineering. *Nat. Mater.* **13**, 796–801 (2014).
- Zhou, H. et al. Interface engineering of highly efficient perovskite solar cells. *Science* **345**, 542–546 (2014).
- Wang, T. et al. Transporting holes stably under iodide invasion in efficient perovskite solar cells. *Science* **377**, 1227–1232 (2022).
- Zhao, D. et al. Boron-doped nitrogen-deficient carbon nitride-based Z-scheme heterostructures for photocatalytic overall water splitting. *Nat. Energy* **6**, 388–397 (2021).
- Low, J., Yu, J., Jaroniec, M., Wageh, S. & Al-Ghamdi, A. A. Heterojunction photocatalysts. *Adv. Mater.* **29**, 1601694 (2017).
- Chen, X. et al. Reversible charge transfer and adjustable potential window in semiconductor/faradaic layer/liquid junctions. *iScience* **23**, 100949 (2020).
- Yin, Z. et al. Mildly regulated intrinsic faradaic layer at the oxide/water interface for improved photoelectrochemical performance. *Chem. Sci.* **11**, 6297–6304 (2020).
- Ren, F. et al. An extrinsic faradaic layer on CuSn for high-performance electrocatalytic CO<sub>2</sub> reduction. *CCS Chem.* **4**, 1610–1618 (2022).
- Wang, P. et al. A capacitor-type faradaic junction for direct solar energy conversion and storage. *Angew. Chem. Int. Ed.* **60**, 1390–1395 (2021).
- Chen, M. et al. Faradaic junction and isoenergetic charge transfer mechanism on semiconductor/semiconductor interfaces. *Nat. Commun.* **12**, 6363 (2021).

14. Zhang, J. et al. A high-voltage solar rechargeable device based on a CoPi/BiVO<sub>4</sub> faradaic junction. *J. Mater. Chem. A* **10**, 1802–1807 (2022).
15. Wang, P. et al. Photovoltage memory effect in a portable Faradaic junction solar rechargeable device. *Nat. Commun.* **13**, 2544 (2022).
16. Xue, M. et al. Bipolarized intrinsic faradaic layer on semiconductor surface under illumination. *Natl. Sci. Rev.* **10**, nrac249 (2023).
17. Ruan, Q. et al. Stored photoelectrons in a faradaic junction for decoupled solar hydrogen production in the dark. *Chem* **9**, 1850–1864 (2023).
18. Yadav, B. S., Badgajar, A. C. & Dhage, S. R. Effect of various surface treatments on adhesion strength of magnetron sputtered bi-layer Molybdenum thin films on soda lime glass substrate. *Sol. Energy* **157**, 507–513 (2017).
19. Gong, Y. et al. Elemental de-mixing-induced epitaxial kesterite/CdS interface enabling 13%-efficiency kesterite solar cells. *Nat. Energy* **7**, 966–977 (2022).
20. Yan, C. et al. Cu<sub>2</sub>ZnSnS<sub>4</sub> solar cells with over 10% power conversion efficiency enabled by heterojunction heat treatment. *Nat. Energy* **3**, 764–772 (2018).
21. Shin, S. W. et al. Phase segregations and thickness of the Mo(S,Se)<sub>2</sub> layer in Cu<sub>2</sub>ZnSn(S,Se)<sub>4</sub> solar cells at different sulfuration temperatures. *Sol. Energy Mater. Sol. Cells* **143**, 480–487 (2015).
22. Wen, X., Luo, W., Guan, Z., Huang, W. & Zou, Z. Boosting efficiency and stability of a Cu<sub>2</sub>ZnSnS<sub>4</sub> photocathode by alloying Ge and increasing sulfur pressure simultaneously. *Nano Energy* **41**, 18–26 (2017).
23. Tay, Y. F. et al. Solution-processed Cd-substituted CZTS photocathode for efficient solar hydrogen evolution from neutral water. *Joule* **2**, 537–548 (2018).
24. Yokoyama, D. et al. H<sub>2</sub> evolution from water on modified Cu<sub>2</sub>ZnSnS<sub>4</sub> photoelectrode under solar light. *Appl. Phys. Express* **3**, 101202 (2010).
25. Wei, Z. et al. Engineering of a Mo/Si<sub>x</sub>N<sub>y</sub> diffusion barrier to reduce the formation of MoS<sub>2</sub> in Cu<sub>2</sub>ZnSnS<sub>4</sub> thin film solar cells. *ACS Appl. Energy Mater.* **1**, 2749–2757 (2018).
26. Gupta, B., Melvin, A. A., Matthews, T., Dash, S. & Tyagi, A. K. TiO<sub>2</sub> modification by gold (Au) for photocatalytic hydrogen (H<sub>2</sub>) production. *Renew. Sustain. Energy Rev.* **58**, 1366–1375 (2016).
27. Michaelson, H. B. The work function of the elements and its periodicity. *J. Appl. Phys.* **48**, 4729–4733 (1977).
28. Dias, P. et al. Transparent cuprous oxide photocathode enabling a stacked tandem cell for unbiased water splitting. *Adv. Energy Mater.* **5**, 1501537 (2015).
29. Yang, Y., Fei, H., Ruan, G., Xiang, C. & Tour, J. M. Edge-oriented MoS<sub>2</sub> nanoporous films as flexible electrodes for hydrogen evolution reactions and supercapacitor devices. *Adv. Mater.* **26**, 8163–8168 (2014).
30. Kondekar, N. P., Boebinger, M. G., Woods, E. V. & McDowell, M. T. In Situ XPS investigation of transformations at crystallographically oriented MoS<sub>2</sub> interfaces. *ACS Appl. Mater. Interfaces* **9**, 32394–32404 (2017).
31. Wu, X. L. et al. Green light stimulates terahertz emission from mesocrystal microspheres. *Nat. Nanotechnol.* **6**, 103–106 (2011).
32. Acerce, M., Voiry, D. & Chhowalla, M. Metallic 1T phase MoS<sub>2</sub> nanosheets as supercapacitor electrode materials. *Nat. Nanotechnol.* **10**, 313–318 (2015).
33. Zheng, J. et al. High yield exfoliation of two-dimensional chalcogenides using sodium naphthalenide. *Nat. Commun.* **5**, 2995 (2014).
34. Wang, G., Zhang, L. & Zhang, J. A review of electrode materials for electrochemical supercapacitors. *Chem. Soc. Rev.* **41**, 797–828 (2012).
35. Shao, Y. et al. Design and mechanisms of asymmetric supercapacitors. *Chem. Rev.* **118**, 9233–9280 (2018).
36. Sherbo, R. S. et al. Accurate coulometric quantification of hydrogen absorption in palladium nanoparticles and thin films. *Chem. Mater.* **30**, 3963–3970 (2018).
37. Jansonius, R. P. et al. Strain influences the hydrogen evolution activity and absorption capacity of palladium. *Angew. Chem. Int. Ed.* **59**, 12192–12198 (2020).
38. Hinnemann, B. et al. Biomimetic hydrogen evolution: MoS<sub>2</sub> nanoparticles as catalyst for hydrogen evolution. *J. Am. Chem. Soc.* **127**, 5308–5309 (2005).
39. Sarkar, S. & Peter, S. C. An overview on Pd-based electrocatalysts for the hydrogen evolution reaction. *Inorg. Chem. Front.* **5**, 2060–2080 (2018).
40. Ding, X., Zhang, L. & Gao, Y. Insights into electrolyte effects on photoactivities of dye-sensitized photoelectrochemical cells for water splitting. *J. Energy Chem.* **26**, 476–480 (2017).
41. Ding, C., Shi, J., Wang, Z. & Li, C. Photoelectrocatalytic water splitting: significance of cocatalysts, electrolyte, and interfaces. *ACS Catal.* **7**, 675–688 (2017).
42. Gong, Y. et al. Identifying the origin of the V<sub>oc</sub> deficit of kesterite solar cells from the two grain growth mechanisms induced by Sn<sup>2+</sup> and Sn<sup>4+</sup> precursors in DMSO solution. *Energy Environ. Sci.* **14**, 2369–2380 (2021).

## Acknowledgements

This work was supported by the National Natural Science Foundation of China (22279052, W. L.), the National Key R&D Program of China (2017YFE0120700, W. L. and 2019YFE0118100, H. X.), the Science and Technology Development Fund from Macau SAR (FDCT 008/2017/AMJ, S. H.-K.).

## Author contributions

W.L. supervised the project, proposed the concept and designed the experiments. H.D. and X.P. carried out sample preparation. H.D. carried out sample characterization and electrochemical measurement. W.L. and H.D. analyzed the data and wrote the paper. Y.G., M.X., P.W., S.H.-K., Y.Y., H.X., W.L. and Z.Z. discussed the results and gave comments on the manuscript.

## Competing interests

The authors declare no competing interests.

## Additional information

**Supplementary information** The online version contains supplementary material available at <https://doi.org/10.1038/s41467-023-43916-6>.

**Correspondence** and requests for materials should be addressed to Hao Xin or Wenjun Luo.

**Peer review information** *Nature Communications* thanks Fatwa Abdi, and the other, anonymous, reviewer(s) for their contribution to the peer review of this work. A peer review file is available.

**Reprints and permissions information** is available at <http://www.nature.com/reprints>

**Publisher's note** Springer Nature remains neutral with regard to jurisdictional claims in published maps and institutional affiliations.



**Open Access** This article is licensed under a Creative Commons Attribution 4.0 International License, which permits use, sharing, adaptation, distribution and reproduction in any medium or format, as long as you give appropriate credit to the original author(s) and the source, provide a link to the Creative Commons license, and indicate if changes were made. The images or other third party material in this article are included in the article's Creative Commons license, unless indicated otherwise in a credit line to the material. If material is not included in the article's Creative Commons license and your intended use is not permitted by statutory regulation or exceeds the permitted use, you will need to obtain permission directly from the copyright holder. To view a copy of this license, visit <http://creativecommons.org/licenses/by/4.0/>.

© The Author(s) 2023